energies

Article

Numerical Study on the Aerodynamics of the Evacuated Tube Transportation System from Subsonic to Supersonic

Zhiwei Zhou [1,2], Chao Xia [1,2,*], Xizhuang Shan [1,2] and Zhigang Yang [1,2,3]

[1] School of Automotive Studies, Tongji University, Shanghai 201804, China; zhouzhiwei@tongji.edu.cn (Z.Z.); shanxz@tongji.edu.cn (X.S.); zhigangyang@tongji.edu.cn (Z.Y.)
[2] Shanghai Automotive Wind Tunnel Center, Tongji University, Shanghai 201804, China
[3] Beijing Aeronautical Science and Technology Research Institute, Beijing 102211, China
* Correspondence: chao.xia@tongji.edu.cn

Abstract: In this study, the aerodynamic characteristics of the three-dimensional evacuated tube transportation (ETT) system based on the Reynolds-averaged Navier–Stokes $\kappa-\omega$ shear-stress transport turbulent model were investigated. The effects of two key parameters on the drag and flow topology of the ETT system, namely the travelling speed and ambient pressure in the tube, were studied. Compared with trains in the atmospheric environment without the tube (i.e., the open system), the ETT system shows considerable drag reduction with suitable operating parameters in the tube, particularly at a higher travelling speed range. The drag varying with the speed from subsonic to supersonic, shows various change trends at different speeds because of their distinct flow structures. The higher pressure in front of train head was observed to be reduced by choking, and a low pressure in the wake by expansion waves led to rapid increase in the drag and drag coefficient. The relationship between the drag and operating pressure was observed to be approximately linear for both the subsonic and supersonic speeds.

Keywords: evacuated tube transportation; numerical simulation; aerodynamic drag; shock wave; supersonic speed

Citation: Zhou, Z.; Xia, C.; Shan, X.; Yang, Z. Numerical Study on the Aerodynamics of the Evacuated Tube Transportation System from Subsonic to Supersonic. *Energies* **2022**, *15*, 3098. https://doi.org/10.3390/en15093098

Academic Editor: Alessandro Bianchini

Received: 11 March 2022
Accepted: 19 April 2022
Published: 24 April 2022

1. Introduction

The rapid development of the modern society has necessitated higher requirements to satisfy the emerging transportation needs. Although the existing means of transportation, including railway, highway, shipping, and air transportation, can meet people's primary demand, they have some inherent problems such as traffic jams, air pollution, noise pollution, security, and economic problems. In this study, the novel evacuated tube transportation (ETT) system was investigated, which has a higher speed, higher security, lower energy consumption, less noise, and less pollution. The basic idea of the ETT system is that the train moves in a closed tube that draws a certain amount of vacuum, and uses maglev technology or compressed air cushion to levitate the train over a certain distance on the track [1–7]. Consequently, almost all of the drag of the train in tubes comes from the aerodynamic drag.

The most economical speed in a dense atmosphere is less than 400 km/h, and the ratio of the aerodynamic drag to the overall driving resistance is more than 80% [8]. Therefore, it is a good choice for a ground vehicle to travel in a certain degree of vacuum in the tube with the maglev technology or compressed air cushion suspension [9–13]. In this way, the aerodynamic drag dominates the overall driving resistance. Hence, it is necessary to research the aerodynamic characteristics of the ETT system to achieve greater performance. After considering the 'Hyperloop Alpha' of Elon Musk, NASA researchers suggested that the ETT system design parameters play important roles in aerodynamic characteristics [14], including the travelling speed of the ETT train, ambient pressure in the tube, blockage ratio between the train and tube, ambient temperature, train length, etc. [4,6,7,15,16].

Edwards [17] put forward a concept that ETT trains travel in a certain degree of vacuum in the tubes at a speed of 224 m/s, which belongs to the subsonic speed at atmospheric temperature. However, the 'Swissmetro' project in Switzerland used a subsonic speed in vacuum tunnels (139 m/s) [18,19]. Although Elon Musk focused on the transonic 'Hyperloop Alpha' [6] and Daryl Oster discussed the feasible speed of the ETT system from 56 to 2083 m/s [20], some teams have proposed tube trains capable of running at 1111 m/s [21]. It is common knowledge that the drag of the tube trains increases as the speed increases. Based on numerical simulation with a $\kappa-\omega$ SST simulation model for a simplified tube train [22], Kim et al. reasoned that the drag of a tube train was not linearly proportional to the square of the speed. Mi et al. used dynamic mesh treatment with the same simulation model to study the drag of a tube train, and obtained results similar to Kim et al. [23]. Ma et al. deduced the formula between the drag and velocity based on basic aerodynamic equations and experiments at extremely low speeds [24]. Jae-Sung Oh et al. observed that the drag significantly increases when the pod reaches the critical Mach number (*Ma*) by studying running speed from 50 to 350 m/s with a steady $\kappa-\omega$ SST simulation model [25]. Le et al. indicates that drag coefficient increases with increase in blockage ratio, pod speed, and pod length from 100 to 350 m/s [26]. Niu et al. observed that the aerodynamic drag coefficient of the tube train first increased and then decreased with increasing speed from 111 to 556 m/s [27]. They also explored the changing process of the drag coefficient existing in the acceleration and deceleration stages [28]. Zhou et al. examined the turning point existing in the relationship between the aerodynamic drag and Mach number from 0.5 to 1.0, and observed that the relationship became linear [29].

Research on the degree of vacuum in the tube of the ETT system is equivalent to investigating the ambient pressure in the tube. The drag of the train increases with increasing ambient pressure in the tube of the ETT system [22,23,25,30,31]. The relationship between the two has been shown to be proportional to each other at subsonic speed [22]. Meanwhile, it has been observed that the drag decreases when the blockage ratio of the ETT system increases [22,23,25,30–32]. However, the effect of a change in the tube length on the total drag was found to be insignificant [25]. Higher ambient temperature results in lower drag because the higher velocity of sound will delay severe choking in the flow [25].

The choking phenomenon usually occurs in the flow with varying area channels, such as the Laval nozzle [33]. When the inlet velocity surpasses the critical Mach number, not all the flux will pass through the minimum cross section of the channel. Therefore, the exceeding gas overstocking in front of the minimum cross-section will lead to a series of aerodynamic problems. Because of the changes in the cross-sectional area caused by the pod trains in the tube, this system can be regarded as a type of nozzle. The choking phenomenon will occur when the incoming flow velocity reaches the critical *Ma* and the flow speed attains the velocity of sound at the minimum cross-section for confirmed blockage ratio [34,35]. No doubt the choking phenomenon can occur in a tube train system with the suitable situation. The critical speed is inversely proportional to the blockage ratio, but the effect of the internal tube pressure is negligible [22]. The total drag of an ETT train will increase significantly after choking [14,25]. For this reason, the 'Hyperloop Alpha' concept proposed installing a compressor at the head of the capsule to weaken the impact of choking [6]. Kim found that installing a compressor at the head of the capsule can reduce the 30% aerodynamic drag at a speed of 600 km/h [36]. Bose provided that adding the aerofoil-shaped fins did good to mitigate the chocking effect and reduced the pressure build-up at the front of the pod in the tube [37]. Moreover, optimizing the shape of the tube trains facilitates drag reduction [30,38–41]. Chen attempted to achieve a lower drag of the tube train by transforming the geometrical shape of the head and tail [30]. Both Opgenoord and Braun optimized the geometrical profile to control the separation of the boundary layer at the head and tail by using genetic algorithm [38,39]. Gillani found that different shapes of head and tail of the train had significantly effects on the drag force of the vacuum train in the tube [40]. A tube train with an axial channel has a small effect on the pressure drag but a large effect on the friction drag [41]. Twin tubes with a cross passage applied to the ETT system are also effective in reducing the pressure drag [42].

Many researchers have studied the aerodynamic characteristics of the ETT system by using Computational Fluids Dynamics (CFD) for their aerodynamic experiments on the ETT system, which is often difficult to realize. In addition, most research conclusions focused on the subsonic and transonic aspects. However, the ETT system has great potential in terms of speed, which includes both the subsonic and supersonic speeds [6,17–20]. The supersonic speed of the ETT system has been mentioned occasionally in some works. Kim considered the supersonic speed, but focused on the results of low velocity; the analysis of flow mechanics was weakly conducted [22]. Although Niu studied the ETT system at 0.33–1.63 of the *Ma*, the work focused more on the impact of the Mach number on the coupling effect of the aerodynamic heating and aerodynamic pressure caused by a tube train [27]. Different travelling speeds cause diverse aerodynamic features. Moreover, a higher speed perhaps leads to a more complex flow structure, which necessitates higher requirements in the design of the ETT system. To the author's best knowledge, the drag reduction in the ETT system at different speeds, compared with the atmospheric environment, is not clear enough in the literature. In addition, the changing law of the drag varies from the subsonic to supersonic speeds, and the corresponding flow mechanics have not been fully understood. These are important to the design speed. Although the linear relationship between the drag and ambient pressure in the tube has been verified at several subsonic speeds, it has not been known in the supersonic range. Furthermore, the impact of various ambient pressure on the flow field is still an open question. Hence, the aerodynamic transformation law of the ETT system from the subsonic to supersonic speeds needs to be studied thoroughly.

This work first compared the aerodynamic characteristics between the ETT system and the open system from 100 to 700 m/s. Then, two key parameters, i.e., the travelling speed and ambient pressure in the tube, were explored from the subsonic to supersonic speeds by analyzing their relationship law in detail, combined with the velocity and pressure features in the flow field.

The remainder of this paper is organized as follows. Section 2 presents details of the methodology employed in this study, including the physical model, the numerical method, the computational grids and sensitivity study, and the numerical validation. Section 3 conducts discussions on the results of the study in terms of the comparison between the ETT and open system, and the key aerodynamic parameters of the ETT system (i.e., the travelling speed and ambient pressure in the tube). Finally, Section 4 provides a concise summary of the study, along with the main findings.

2. Numerical Set-Up

2.1. Physical Model

In previous studies, there was no uniform choice for the shape of the pod train in the ETT system. However, a simple model proved more beneficial to investigate the basic aerodynamic characteristics of this system. Therefore, a simple pod train was modelled in this study after considering the models in previous studies [22,25–28,30]. As illustrated in Figure 1a, a full-scale pod train model placed on the axis of a vacuum tube was chosen, and it consisted of a cone head (train head), a cylinder pod body (train carriage), and a cone tail (train tail). The pod train is 15.88 m in length (L) and 3 m in diameter (d_{tr}), whereas the vacuum tube is 6 m in diameter (d_{tu}).

The computational domain is 616 m in length (about 39 L) and 6 m in diameter tube; the details are shown in Figure 1b. The distance between the inlet and the nose tip of the train head is approximately 19 L, which is the same as the distance from the nose tip of the train tail to the outlet.

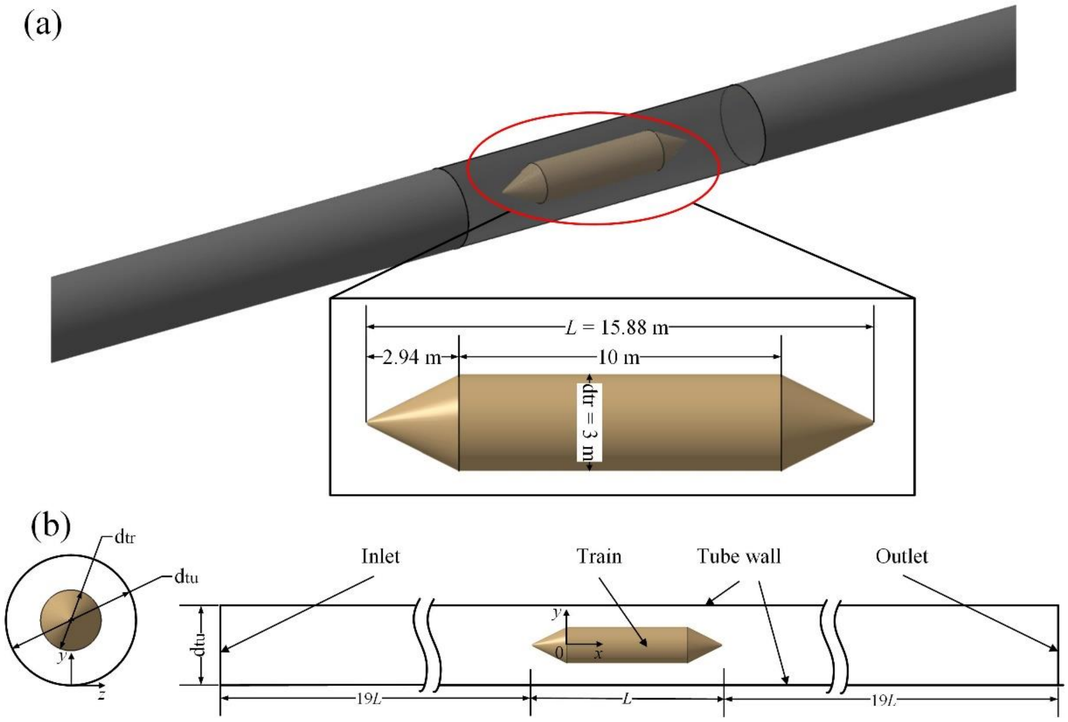

Figure 1. (**a**) Three-dimensional diagram of the ETT system, (**b**) Two-dimensional diagram of the computational domain.

2.2. Numerical Method

Because of the high speed and Reynolds number involved in this study, a viscous and compressible steady-state turbulence flow model was employed. The $\kappa-\omega$ SST and realizable $\kappa-\varepsilon$ turbulent models are mainly used to investigate the ETT aerodynamic characteristics, which have proven to be reliable [22,23,25,27,30,31,39]. Thus, the Reynolds-averaged Navier–Stokes (RANS) $\kappa-\omega$ SST model based on a density-based implicit solver in the commercial software FLUENT 19.2.0 was utilized in this study, which is well in simulating separation flow [43]. Roe-FDS was selected for processing the flux type. Gradients were computed with using a least-squares approach in control volumes surrounding the cells. The second-order upwind was used to the spatial discretization. The ideal gas with Sutherland viscosity setting was selected for the fluid material in the simulation. The pressure far filed inlet and outlet with no-reflection of wave were involved, which required far-enough distance from the object of interest. The assumption of the stationary wall and moving wall with no-slip shear condition were employed for the pod train surface and tube wall, respectively.

A series of cases with various speeds at the inlet were conducted in this study, including U = 50, 100, 150, 175, 200, 250, 300, 350, 400, 500, 600, and 700 m/s (corresponding to Ma = 0.144, 0.288, 0.432, 0.504, 0.576, 0.720, 0.864, 1.008, 1.152, 1.440, 1.728, and 2.016, respectively). The hydraulic diameter D_h has a relation ($D_h = d_{tu} - d_{tr}$), which was determined to be 3 m. The Reynolds number (Re) was calculated using the parameters ρ (density), U (travelling speed), D_h and μ (viscosity). The tube pressure was set to 10,132.5 Pa, equal to 0.1 times the magnitude of the standard atmospheric pressure (0.1 atm). The parameter ρ can be obtained easily based on the relation between the pressure and density. According to the function $Re = \rho U D_h/\mu$, it ranges from 9.86×10^5 to 1.38×10^7.

To explore the impact of ambient pressure in the tube on the aerodynamics of the ETT system, pressures at 0.001, 0.005, 0.01, 0.05, 0.1, 0.5, and 1 atm were simulated in this study. For the tube's ambient situation with such low operating pressure, whether the function of continuity in the simulation model can be applied should be discussed. The Knudsen number (Kn) can be used to describe how sparse the gas is. The Kn is defined as follows:

$$Kn = \frac{k_B T}{\sqrt{2}\pi d_m^2 P l} \tag{1}$$

where k_B is Boltzmann constant and d_m is the diameter of a gas molecule, and l is the characteristic length. When $Kn > 0.01$, the continuum model is no longer suitable for flow calculation [44]. Assuming $d_m \approx 3.5 \times 10^{-10}$ m, then Kn varies from 2.5×10^{-8} to 2.5×10^{-5} when the operating pressure changes from 1 atm to 0.001 atm. Hence, the simulation model mentioned above can still be applied.

2.3. Computational Grids and Sensitivity Study

The topology of the computational grid is the cutcell, which can generate a high percentage of perfect hexahedron elements, and is less numerically dissipative in CFD simulations. It also reduces cell counts for the same resolution of hexcore or tetrahedral meshes due to the high percentage of hex elements. The prism layer connects the body surface and the core zone of the grids, where $y+$ is controlled at ~5 in this study. The sensitivity study was performed on three different grids with different number of cells: coarse, medium, and fine grids consisting of 17.53 million, 27.82 million, and 38.33 million cells, respectively. Figure 2a shows the distribution of the medium grid around the pod train, where the maximum cell size is ~256 mm lying in the peripheral area of the computational domain. The grid is refined with sizes 128 mm for the coarse mesh on the wake region and pod surrounding region. It is refined with size 64 mm for the medium mesh. The same refinement is set with larger block for the fine mesh. Cases with different speeds were simulated with different meshes for their different prism setting to ensure the $y+$.

Cases with subsonic travelling speed (200 m/s) and supersonic travelling speed (400 m/s) were calculated to investigate the mesh sensitivity. As shown in Table 1, compared with the fine mesh results, the deviations in the total drag are −0.10% and 0.14% for the coarse and medium grids, respectively, in the 200 m/s case. These are −0.06% and 0.10%, respectively, for the 400 m/s case. Overall, the deviation in the drag results for the three sets of grids is less than 1% from each other. As shown in Figure 2b, the three grids present good agreement with each other on the distribution of pressure coefficient. Considering the costs and accuracy of simulation, the medium mesh setting was applied in this study.

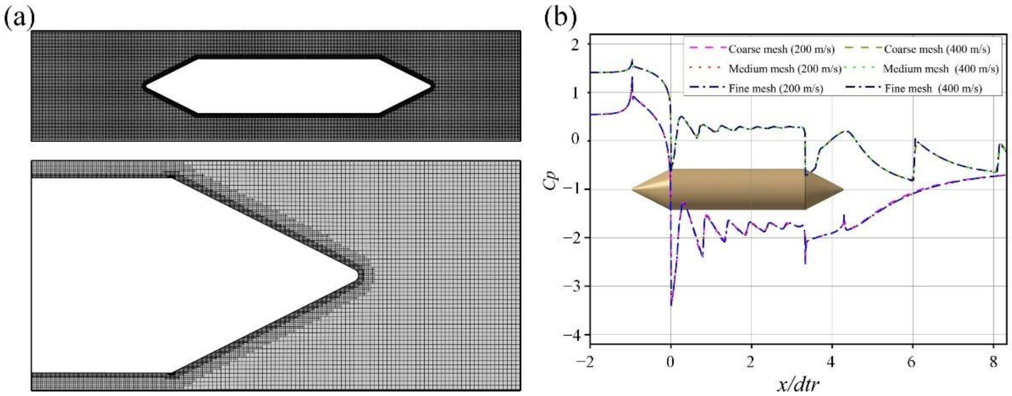

Figure 2. (**a**) Grids around the pod train, (**b**) the distribution of pressure coefficient along the axis of the tube and the longitudinal line on the train surface of the three grids.

Table 1. Spatial resolution and drag for coarse, medium, and fine grids.

MESH	Coarse	Medium	Fine
Cell number (million)	17.53	27.82	38.33
Total drag_200 m/s (N)	38,587.20	38,496.20	38,549.16
Error (with fine mesh)	−0.10%	0.14%	-
Total drag_400 m/s (N)	108,249.55	108,076.80	108,189.74
Error (with fine mesh)	−0.06%	0.10%	-

2.4. Numerical Validation

In order to verify the accuracy of the numerical method in this work, the flow around a waisted body of revolution running at different speeds from the subsonic to supersonic speeds [45] was simulated due to the lack of the aerodynamic experiment result for a tube train, which is still in the conceptual design stage at the moment. The same numerical sets in the above ETT system simulation were used in the waisted body cases. The computational domain and boundary conditions are shown in Figure 3, where the pressure far-field boundary condition is applied for all the boundaries except the surface of the waisted body of revolution. The stationary wall represents the wall boundary. The cutcell method was also employed to generate the grids as shown in Figure 4. The prism layer was connected to the body surface and the core zone of the grids.

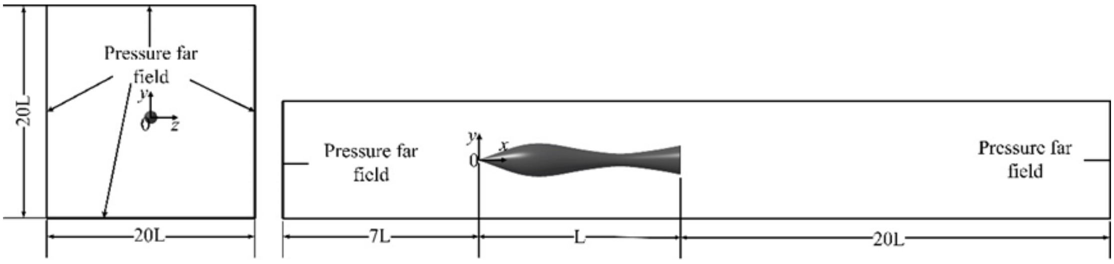

Figure 3. Two-dimensional diagram and boundary setting of the computational domain for the waisted body.

Figure 5 presents the distribution of pressure coefficient (C_P) along the longitudinal symmetry line over the model's upper surface for both RANS $\kappa - \omega$ SST simulation and its wind tunnel experiment [45]. The C_P is defined in Equation (1), where P is the time-averaged surface pressure and P_∞ is the static pressure.

$$C_P = \frac{P - P_\infty}{\frac{1}{2}\rho U^2} \tag{2}$$

The drag coefficient (C_d) is defined as follows:

$$C_d = \frac{D}{\frac{1}{2}\rho U^2 A_x} \tag{3}$$

where D is the total drag, ρ is density, U is travelling speed, and A_x is the projected area in the direction of x.

It is consistent with the numerical simulation and wind tunnel test in C_P at either subsonic or supersonic speed. This implies that the numerical method in this paper is reasonable for simulating the shock wave and expansion wave which occurs for both the tube train and waisted body. Therefore, it was adopted for the numerical simulation in this study because of the similarity in their running speeds and Reynolds numbers.

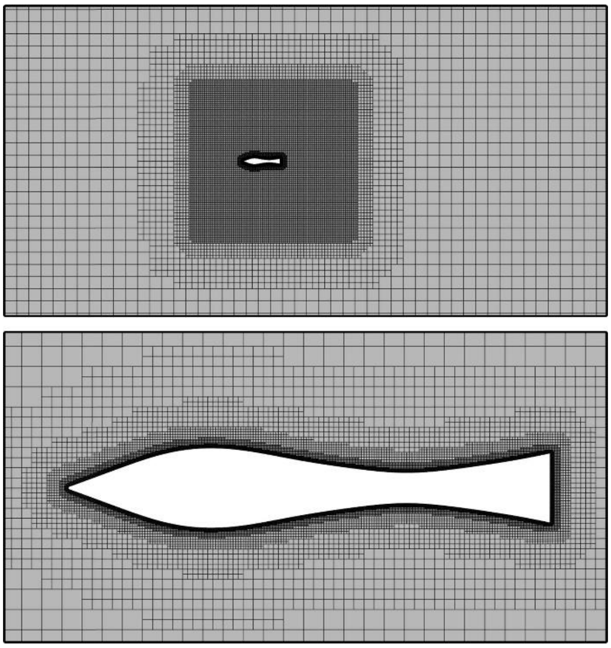

Figure 4. Grids distribution of the waisted body cases.

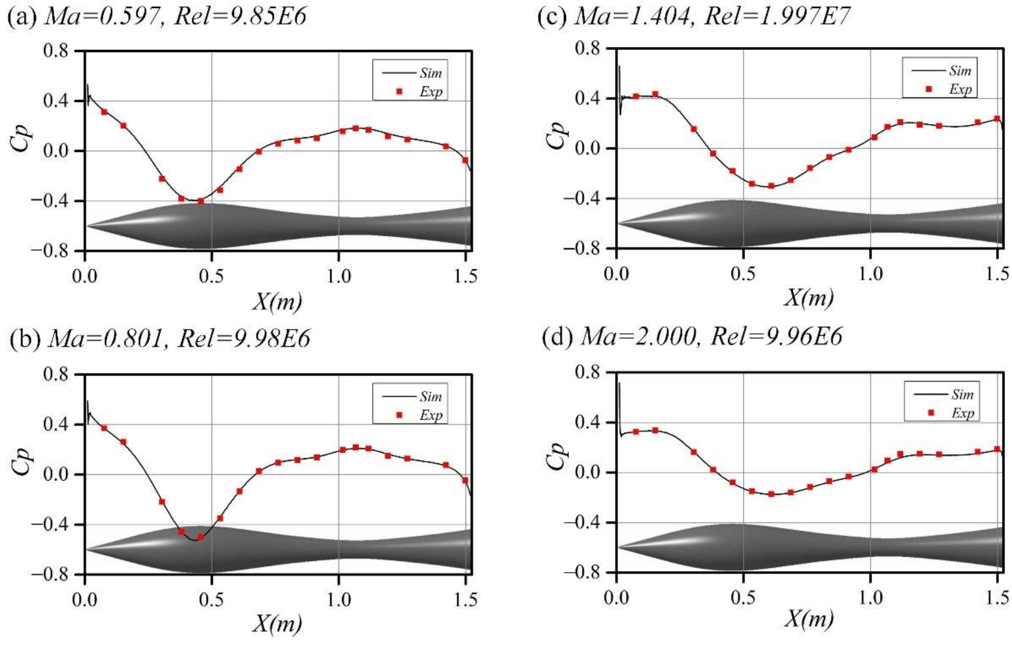

Figure 5. Comparison of the simulation and experimental C_P along the longitudinal symmetry line over the upper surface of the waisted body: (**a**) *Ma* = 0.597, *Re* = 9.85 × 10^6, (**b**) *Ma* = 0.801, *Re* = 9.98 × 10^6, (**c**) *Ma* = 1.404, *Re* = 1.997 × 10^7, (**d**) *Ma* = 2.000, *Re* = 9.96 × 10^6.

3. Result and Discussion

3.1. Comparison between the ETT and Open System

3.1.1. Drag of the Tube Train

To assess the superiority of the ETT system, the drag of the pod train travelling in the atmospheric environment (1 atm) without the tube (open system) has been simulated as the reference. Figure 6a shows the tendency of the aerodynamic drag to vary with increasing travelling speeds for both the ETT (0.1 atm and 0.01 atm) and the open systems. The drag in the three cases increase as the speed increases from 100 to 700 m/s. Meanwhile, the drag in the open system exceeds those in the cases of the 0.1 atm and 0.01 atm ETT system at almost all the speeds.

Figure 6b reveals the drag reduction ratio of the ETT system to the open system. For the 0.1 atm ETT system, approximately half of the drag is reduced at 100 m/s and 300 m/s. However, what stands out in the figure is the 4.9% at U = 200 m/s. This suggests that the drag reduction contributed by the low air pressure in the tube is insufficient to counteract the negative impact of the ETT system in this situation. Significant differences in the flow structure between the open system and 0.1 atm ETT may be the main cause of the low drag reduction at this speed, as shown in Section 3.1.2. Drag reductions from U = 400 to 700 m/s show close values, which are all higher than 80%. This confirms the economy and energy-saving feature of the ETT system.

For the 0.01 atm ETT, the drag reduction maintains a high level from 90% to 98%, but slightly drops to 90.69% at 200 m/s in Figure 6b. Above all, the ETT system shows a considerable drag reduction effect with suitable operating parameters. This means that the ETT system has great superiority in high-speed ground transportation.

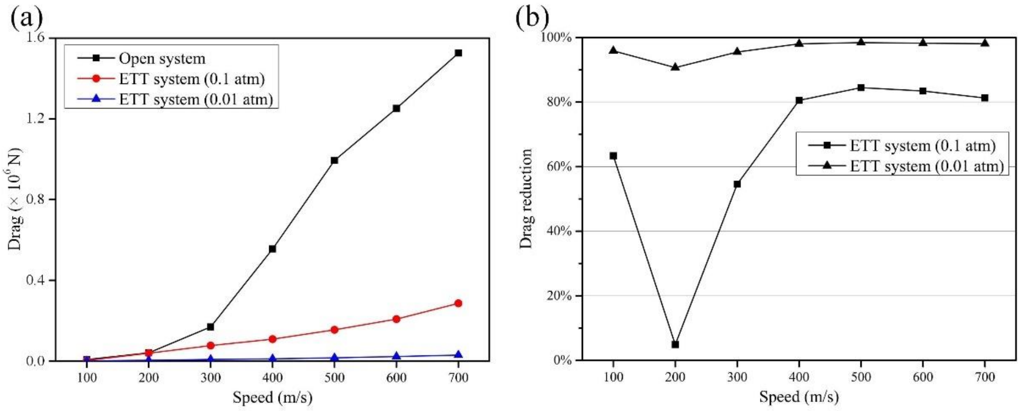

Figure 6. (**a**) Drag of the tube train for the 1 atm open system, 0.1 atm ETT system, and 0.01 atm ETT system from U = 100 to 700 m/s, (**b**) Drag reduction in tube trains compared with the 1 atm open system.

3.1.2. Flow Topology

The flow field around the train can be divided roughly into five parts, i.e., zone I, II, III, IV, and V, as shown in Figure 7. The comparison of Mach number contours in the (x, z) plane at $y = 0$ between the open system and the 0.1 atm ETT system are shown in Figure 8 for U = 100, 200, 400, and 600 m/s. The color bar threshold value in each case is adjusted appropriately to make the feature of flow structures more obvious. Specifically, the flow structure of the two systems has no significant change. Note that the minor differences between the two systems at U = 100 m/s exist in zone III, IV, and V, as presented in Figure 8a,e. The effect of the tube wall on the flow field significantly speeds up the Ma in zone III of the 0.1 atm ETT system. The other difference is included in the size of the dead zone in the wake of the train.

In contrast to the U = 100 m/s case, the obvious distinction between the two systems is evident in the cases of U = 200, 400, and 600 m/s. For U = 200 m/s, low Ma caused by choking in front of train head, waves reflection around the train carriage, and expansion waves in the near wake play a significant role in the ETT flow field (Figure 8b), but do not exist in the open system (Figure 8f). As for U = 400 m/s and 600 m/s, choking also occurs in front of the train head in the ETT system (Figure 8c,g) instead of a detached shock wave and attached shock wave in the open system (Figure 8d,h). Waves reflection and intersection can also be seen in the wake of the ETTs for both U = 400 m/s and 600 m/s, which are not observed in the open system.

From the results above, the flow structures around the train have no significant change at low-speed conditions between the two systems. However, great variations in nature will occur as the speed increases and the choking phenomenon occurs. In addition, high pressure caused by the choking phenomenon in front of the train head and the low pressure caused by the expansion waves at the wake of the train can lead to enormous drag addition. This can offset the drag reduction caused by reducing the ambient pressure in the ETT tube in some speed situations, such as the U = 200 m/s case in the ambient pressure of 0.1 atm, as seen in the pressure distribution shown in Section 3.2.1.

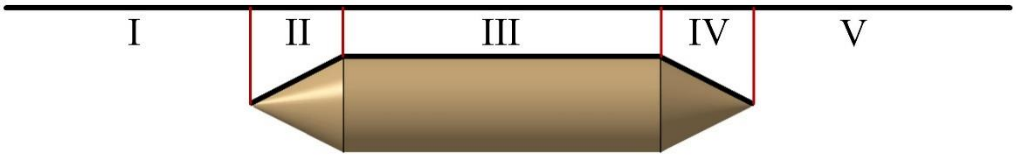

Figure 7. Schematic diagram of partition for flow field in the tube.

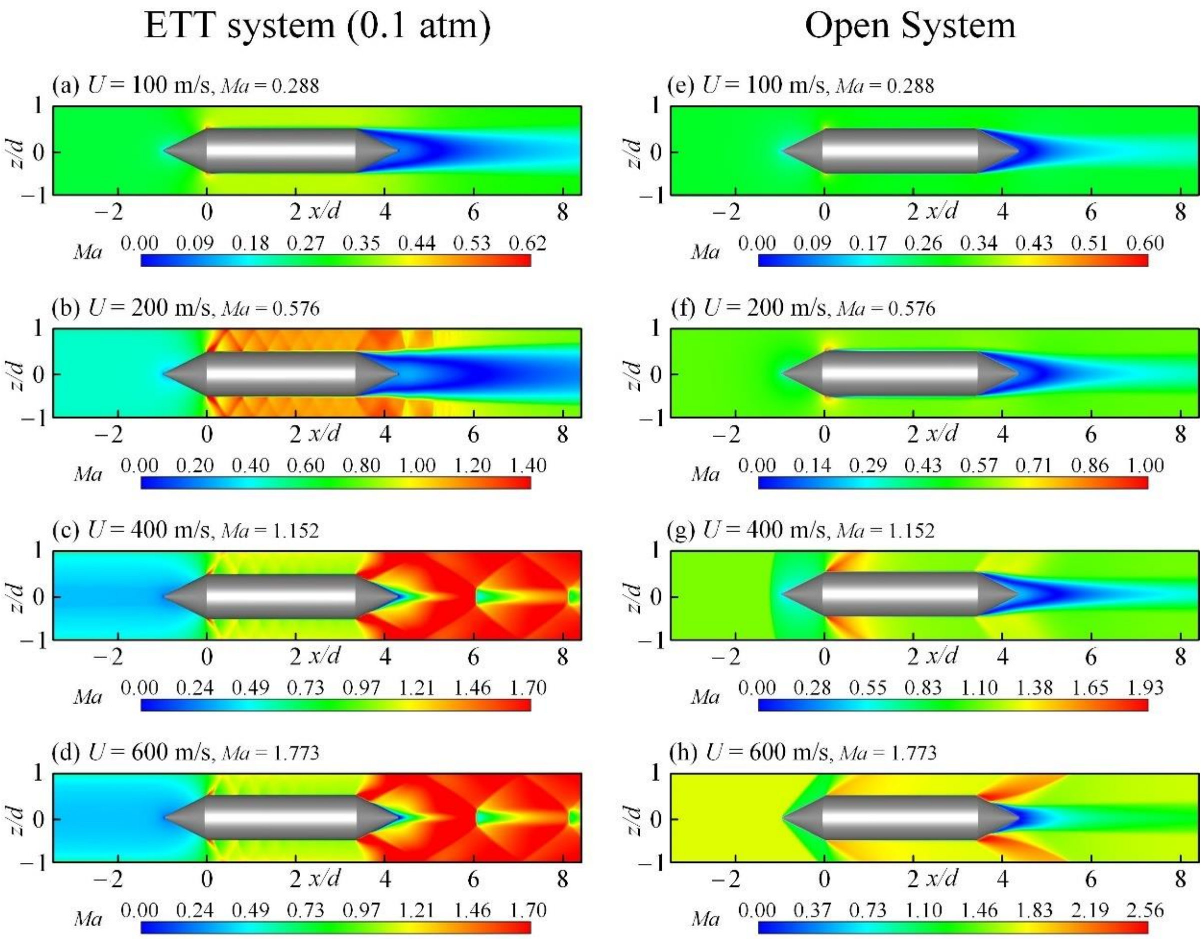

Figure 8. Mach number contours in the (x, z) plane at y = 0: 0.1 atm ETT system (**Left**) and 1 atm open system (**Right**).

3.1.3. Pressure Distribution

Figure 9a,b present the distribution of the C_P along the axis of the tube and the longitudinal line on the train surface for the ETT system and open system, respectively. As shown in Figure 9a, the C_P value in front of the train head increases gradually from 100 to 600 m/s because choking occurs at three higher speeds. As wave reflection takes place around the train carriage for the three higher speeds, there is a certain vibration of the C_P. A low pressure is found in the near wake, which is induced by the expansion wave on the tail train confirmed in Figure 8. Because of the regular wave structures in the wake, the C_P at these places exhibits regular variation at 400 m/s and 600 m/s cases.

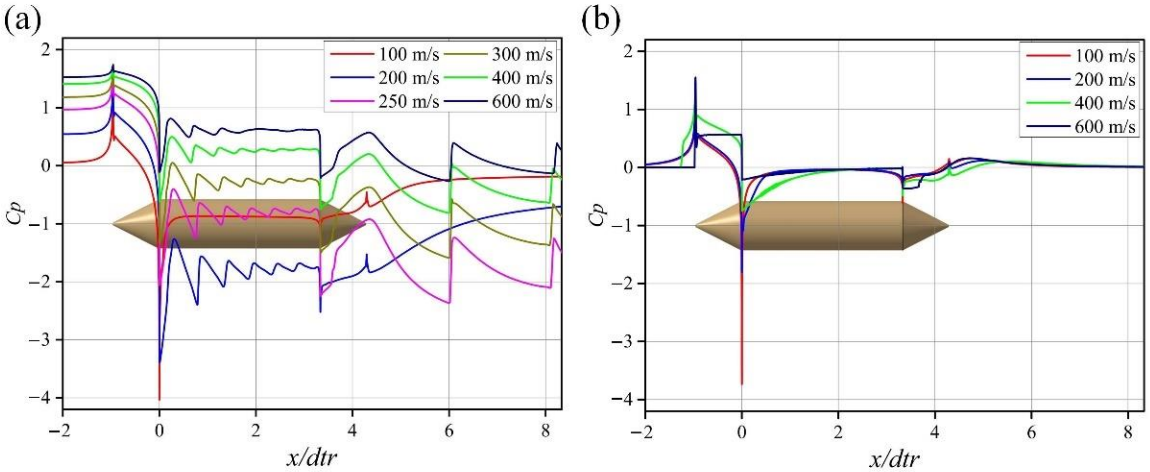

Figure 9. The distribution of pressure coefficient along the axis of the tube and the longitudinal line on the train surface: (**a**) 0.1 atm ETT system, (**b**) 1 atm open system.

As shown in Figure 9b, the C_P curve at the speed of 100 m/s presents a similar changing situation to that of the ETT, except the value in the wake region. The curves of the 200, 400 and 600 m/s, presented in Figure 9b, are different from those of the ETT system due to the diverse flow structures in both systems, which were analyzed in Section 3.1.2.

Together these results provide important insights into both systems: mainly that they share similar aerodynamic characteristics at low travelling speeds, except at the wake zone. Nevertheless, essential differences occur in the two systems at high running speeds due to the existence of the tube. This implies that the train travelling in a tube causes new aerodynamic problem by its special flow structure, which presents challenge in designing the ETT system.

3.2. The Key Aerodynamic Parameters for the ETT System

3.2.1. The Travelling Speed

To explore the effect of the travelling speed on the aerodynamic characteristics of the train from the subsonic to supersonic speeds, a series of cases with various speeds at the inlet were examined in this study. The high *Re* conditions observed suggest that complicated flow structures occur in these cases.

Figure 10a reveals the increasing tendency of the total drag, pressure drag and friction drag of the train. The total drag increases slightly at the initial stage when the travelling speed is relatively slow (from U = 50 to 150 m/s). For U > 150 m/s where the chocking takes place based on the isotropic theory [33], a rapid increase in the drag occurs, and it builds up sharply from U = 175 to 200 m/s. Subsequently, the rate of the drag increase reduces gradually from U = 200 to 350 m/s, similar to the results obtained by Sung [25]. The drag behavior that exceeds the supersonic speed (U > 350 m/s) is different from that of the subsonic speed; the rate of the drag increase rises again, with no critical change, whereas the total drag is linearly related to the travelling speed. In particular, the pressure drag (D_p) has the same variation tendency with the total drag, as the red dotted line shows. Figure 10b shows that the pressure drag occupies a high proportion of the total drag, which ranges from 87.78% to 98.25% when the speed varies from 50 to 700 m/s. This indicates that the pressure drag dominates the drag of the train irrespective of whether the speed is subsonic or supersonic, but it is especially remarkable in the transonic and supersonic speeds. The friction drag (D_f) just increases moderately with increasing speed and it occupies no more than 12.22% of the total drag.

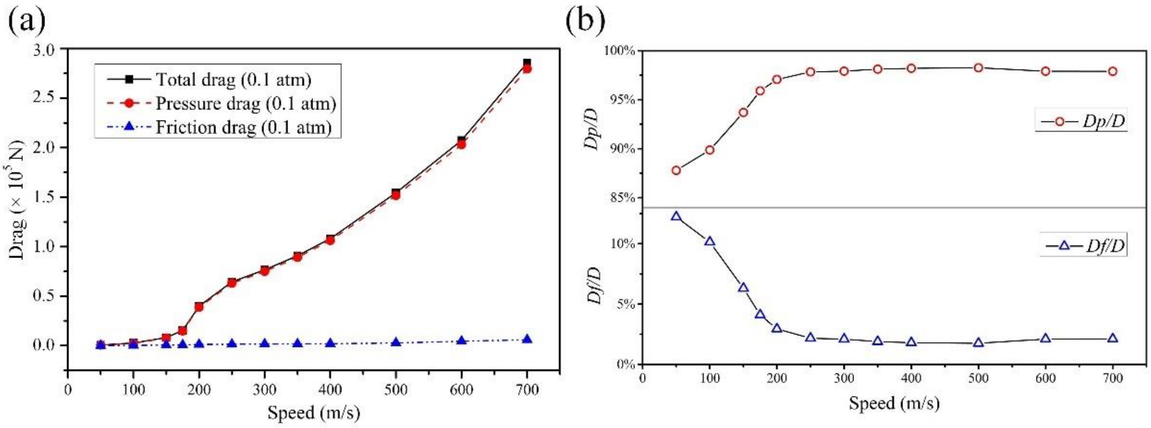

Figure 10. (**a**) Relationship between the drag and travelling speed of the tube train at 0.1 atm, (**b**) percent of pressure drag to total drag and percent of friction drag to total drag at 0.1 atm.

Figure 11 shows that the drag coefficient of the tube train at 0.1 atm varies with travelling speed. It can be observed that C_d is not a determined value as it first rises and then falls afterward. During the rising period, its value climbs tardily in the initial stage of the C_d curve. Then, it comes across the climbout with multiple growths when the speed ranges from U = 175 to 200 m/s, corresponding to the sharp building-up of the total drag exhibited in Figure 10. It can thus be suggested that some different flow structure may appear in this speed region. Of interest is that C_d attains its maximum value (C_{dmax} = 2.48) at U = 250 m/s (Ma = 0.72), and a similar peak value was found at Ma = 0.72 by Le et al. [26] and at Ma = 0.65 by Niu [27]. The C_d curve drops gradually afterward and was almost constant at a value slightly less than 1.5.

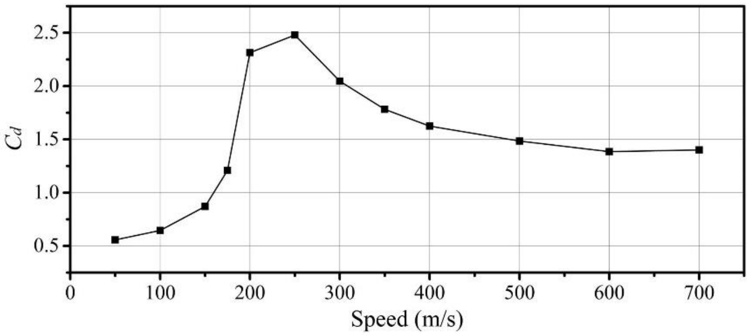

Figure 11. Relationship between the drag coefficient and travelling speed.

The Mach number contours in the (x, z) plane at y = 0 covering the partial area in front of the train and its wake region are shown in Figure 12a–f, which correspond to the cases of 150–600 m/s, respectively. Figure 13 shows the corresponding pressure contours. Note that variational flow structures offer anastomotic evidence for the several stages of the curves in Figures 10 and 11. As is obvious from Figure 12a that the choking has not occurred, this case corresponds to the sluggish addition process in the drag and C_d curves. The flow reveals no obvious change before it reaches the train and maintains the subsonic incoming speed, i.e., the flow is subcritical. When the flow reaches the train, a stagnation point region can be observed at the nose of the train head. Thereafter, the flow speeds up gradually in zone II because the flow channel narrows down. The maximum Ma occurs at the joint of the train head and train carriage where the end of the converging section exists between the train-head wall and the tube wall. The flow moves past the train carriage at a high speed in zone III. Then, it slows down and returns to the incoming velocity due to the expansion of the flow channel in zone IV. There is a dead-water zone in the near wake region, corresponding to the low-pressure region formed in the wake in Figure 13a.

It can be seen from Figure 12b that the velocity of the flow in front of the train is lower than the travelling speed. This indicates that the choking phenomenon, which usually takes place in the flow at the varying-area channels, has occurred in this case. Because the inlet velocity has surpassed the critical Mach number of this system, the exceeding gas overstocking in front of the train leads to a slowdown stream and increased pressure. It is obvious that the pressure in front of the train head has a significant influence in the 175 m/s case compared with the 150 m/s case, as shown in Figure 13a,b. Therefore, the rapid increase in the drag/C_d from 150 to 175 m/s can be ascribed to the occurrence of choking.

In Figure 12c, the *Ma* contour of the 200 m/s case is rather different from those of the 150 and 175 m/s cases. The velocity of the flow in zone I is lower than its travelling speed (*Ma* = 0.576), which means that the choking phenomenon has also occurred in this case. However, its pressure in front of the train is higher than the 175 m/s case as shown in Figure 13b,c, which implies that choking is much worse in the 200 m/s case. Note that the sonic velocity occurs at the joint of the train head and carriage. In zone II, the direction of partial flow is parallel to the surface of the train head, so the area at the beginning of zone III is expanded for the flow coming from zone II. Therefore, its speed continues to increase up to the supersonic velocity from sonic velocity, where a series of expansion waves occur. The compression waves follow on the heels of the expansion waves, and this leads to a slowdown in the flow. Wave reflections from the expansion and compression waves occur when they encounter the tube and train surfaces at zone III. As can be seen from zone IV, a new expansion wave takes place in this area for the increasing channel area near the train tail. The superposition of the new expansion wave and the reflection waves generates a strong low-pressure area in zone IV, as depicted in Figure 13c. Therefore, the sharp addition of the drag/C_d at the speed of 200 m/s can probably be attributed to two main factors: one is the increasing pressure in front of the train head caused by the higher choking; the other factor is the strong low pressure in the near wake of the train tail due to the expansion waves.

Figure 12d demonstrates that the 250 m/s case has a similar flow topology with the 200 m/s case in zone I, II, and III, namely that choking phenomenon and wave reflection appear in the corresponding zones. Differences can be seen in the wake of the train flow field, where more regular flow structures are displayed compared with the cases mentioned before. Expansion wave occurs in zone IV because of the increasing channel area, and it results in the sequential acceleration and low pressure of the flow as shown in Figures 12d and 13d. Because of the high backpressure, a strong shock wave appears behind the expansion wave in zone IV, which causes mutational speed deceleration and rise in pressure. Of further interest is that wave reflection and intersection occur in the downstream wake field, which forms regular wave structure. This structure weakens gradually further in the field due to the viscidity effect and total pressure losses.

A similar flow structure is demonstrated among the cases from 250 to 700 m/s, although only the contour of 250 m/s, 400 m/s, and 600 m/s are shown in Figures 12 and 13. This suggests that the choking phenomenon has occurred in all these cases, and this will result in a serious increase in the drag as described earlier. As shown in Figure 9a, similar C_P distribution are observed in these cases, and the C_P value in front of the head increases with higher speed. However, the biggest pressure drop gradient at the tail (*x/dtr* = 3.33) is found at 250 m/s, which leads to the strongest expansion wave. This should be the reason for the maximum C_d at this speed.

(a) $U = 150$ m/s, $Ma = 0.432$

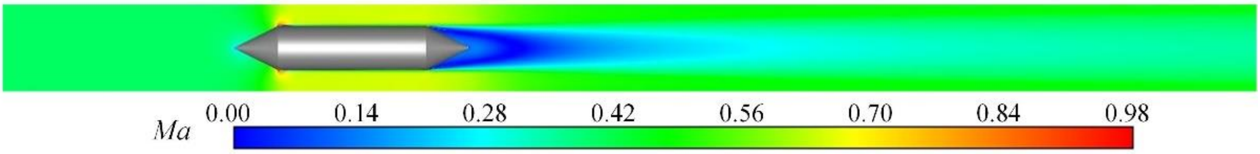

(b) $U = 175$ m/s, $Ma = 0.504$

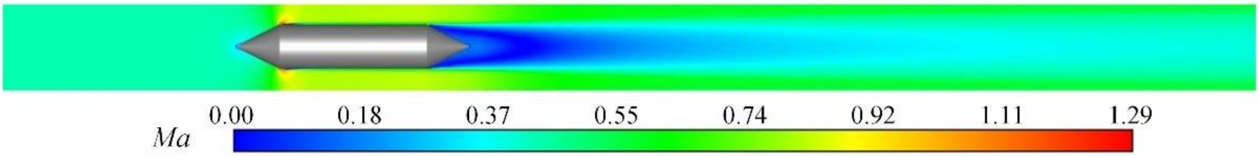

(c) $U = 200$ m/s, $Ma = 0.576$

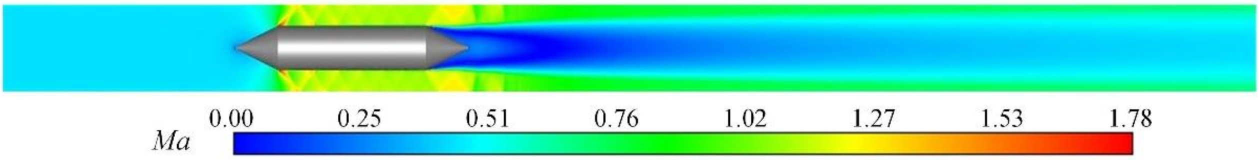

(d) $U = 250$ m/s, $Ma = 0.720$

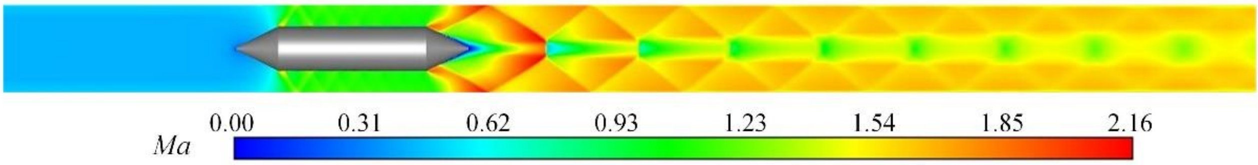

(e) $U = 400$ m/s, $Ma = 1.152$

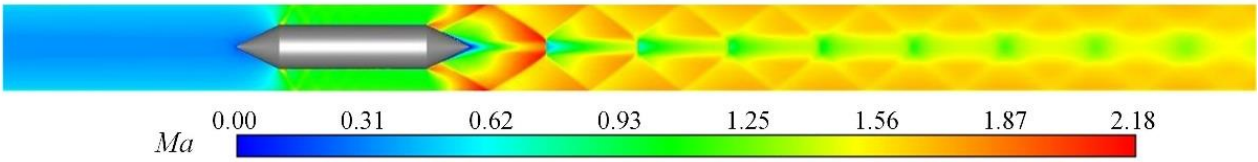

(f) $U = 600$m/s, $Ma = 1.773$

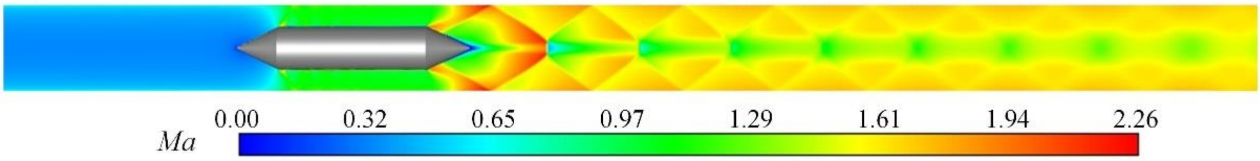

Figure 12. Mach number contours in the (x, z) plane at $y = 0$.

In all, the drag of the tube train varying with the travelling speed demonstrates different variation tendencies in different speed cases from the subsonic to supersonic speeds. Hence, the relationship between the drag and travelling speed of tube trains can be divided into several range of speed to be elucidated. For this reason, the concept of designing the ETT system with different travelling speeds should be adopted.

(a) $U = 150$ m/s, $Ma = 0.432$

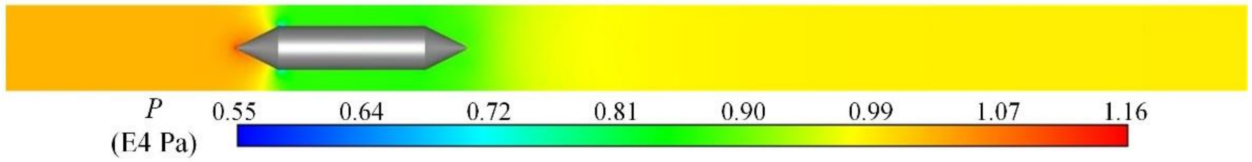

(b) $U = 175$ m/s, $Ma = 0.504$

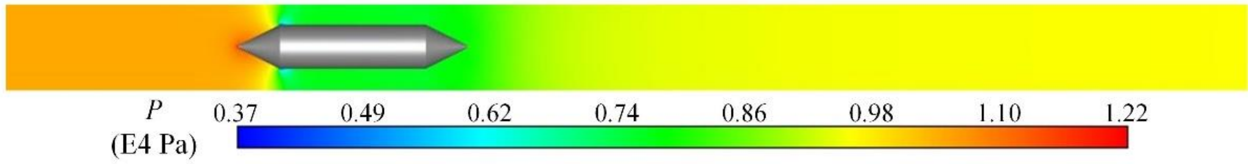

(c) $U = 200$ m/s, $Ma = 0.576$

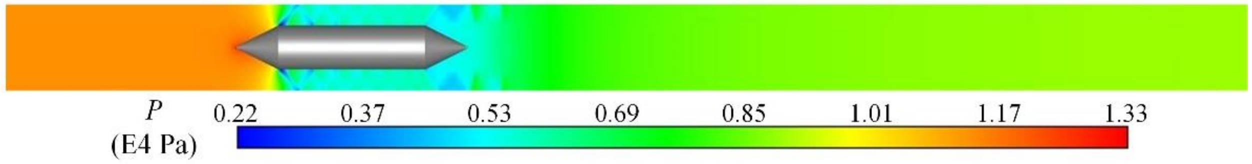

(d) $U = 250$ m/s, $Ma = 0.720$

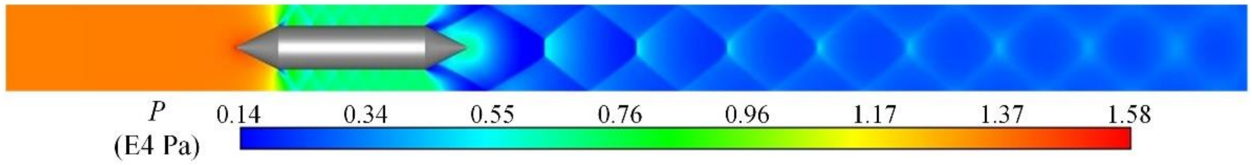

(e) $U = 400$ m/s, $Ma = 1.152$

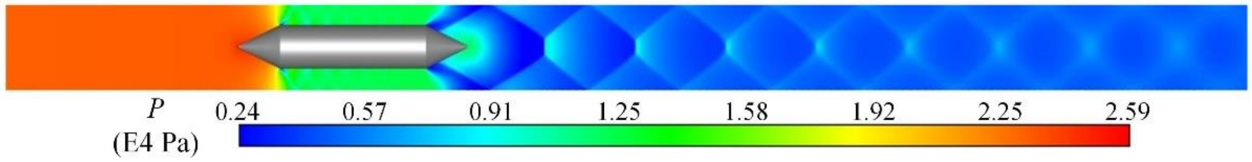

(f) $U = 600$ m/s, $Ma = 1.773$

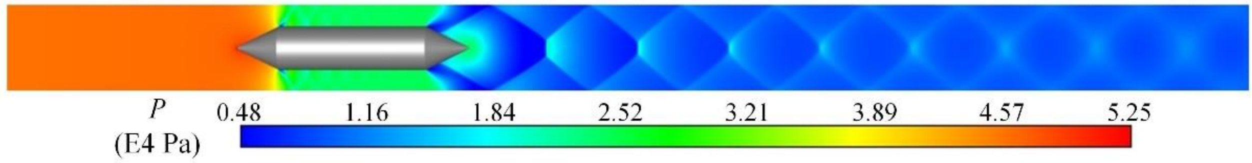

Figure 13. Pressure contours in the (x, z) plane at $y = 0$.

3.2.2. The Ambient Pressure in the Tube

Ambient pressure in the tube at 0.001, 0.005, 0.01, 0.05, 0.1, 0.5, and 1 atm were simulated in this study. As shown in Figure 14a, for the 200 m/s case, the relationship between the drag and ambient pressure is approximately linear (with the slope factor ≈ 3.67), similar to the finding in Kim's study [22]. The linear relationship observed in this research, likewise, is found at a supersonic speed of 400 m/s (with the slope factor ≈ 10.63), as shown in Figure 14b. The relationship between the drag and ambient pressure demonstrates linear features not only in the subsonic speed but also in the supersonic speed.

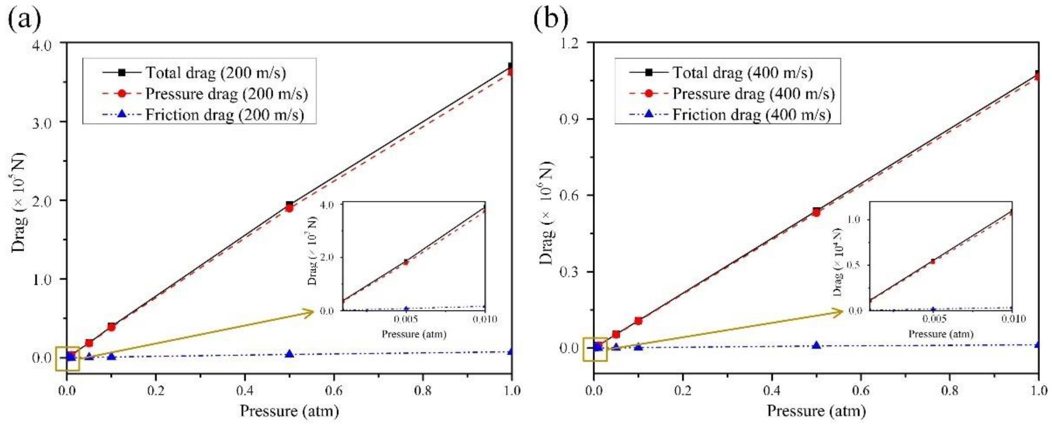

Figure 14. Relationship between the drag and ambient pressure in the tube: (**a**) 200 m/s, (**b**) 400 m/s.

Figure 15 illustrates the relationship between the drag coefficient and ambient pressure in the tube at 400 m/s. It shows that the C_d at the 400 m/s case decreases with increasing ambient pressure in the tube. According to Equation (3), if C_d is constant, the drag of the tube train will be proportional to the reference pressure. The variational C_d indicates that the relationship between the drag and pressure shown in Figure 14b is not strictly linear.

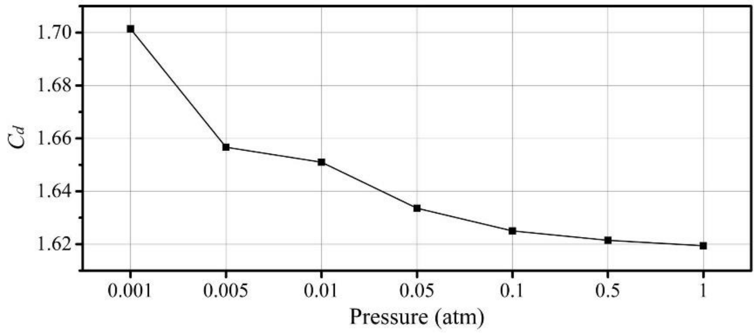

Figure 15. Relationship between the drag coefficient and ambient pressure in the tube at 400 m/s.

Figure 16 displays the comparison of pressure coefficient along the axis of the tube and the longitudinal line on the train surface from 0.001 atm to 1 atm ambient pressure in the tube at a travelling speed of 400 m/s. The C_P curves show a high degree similarity in front of the train head and in the wake of the train tail, which indicates that similar flow structures take place in these areas for different pressure cases. The extremely high pressure occurs in front of the train head, due to the choking phenomenon described in the previous section, for all the pressure setting cases. Note that the data in the wake show the same fluctuation, which means that a series of similar wave structures have taken place as well. Therefore, the approximately linear relationship between the drag and ambient pressure that was clarified earlier is reasonable. Moreover, some distinctions can be found in these similar areas. In front of the train head, the C_P increases gradually as the ambient pressure reduces from 1 atm to 0.001 atm, as shown in Figure 16b. This suggests that lower ambient pressure may contribute relatively more to the strength of the choking. Figure 16c reveals the amplification detail of the C_P in the near wake (especially on the surface of the train tail), where there is a sharp increase in the C_P because a shock wave occurs there. This sharp increase occurs earlier at lower ambient pressure, which means that lower ambient pressure in the tube may cause shock waves faster at this speed near the wake. However, the C_P magnitude appears in an inverse proportion after the shock wave.

The most obvious difference can be verified on the train carriage, as depicted in Figure 16a. The C_P magnitude fluctuates around the carriage for cases of 0.05, 0.1, 0.5, and 1 atm. This implies that the wave reflection occurs around the whole train carriage in zone

III, combined with the striped C_P contour of the train surface shown in Figure 17d–g. However, some distinctions are observed in the amplitude and wavelength of each fluctuation in the latter half in Figure 16a. In contrast with cases from 0.05 to 1 atm, the fluctuation disappears in the latter half surface of the train carriage in the 0.005 atm case due to the break-off of the wave reflection, as represented in Figure 17b. Distinguished from all the other cases, the C_P value fluctuation cannot be observed in the carriage zone for 0.001 atm without wake reflection, but its magnitude is higher than those of the other cases. However, the drag of the tube train is dominated by the pressure drag, and the transformation of the flow structures in zone III contributes little to the total drag. These differences shall be the reason for variational C_d in Figure 15.

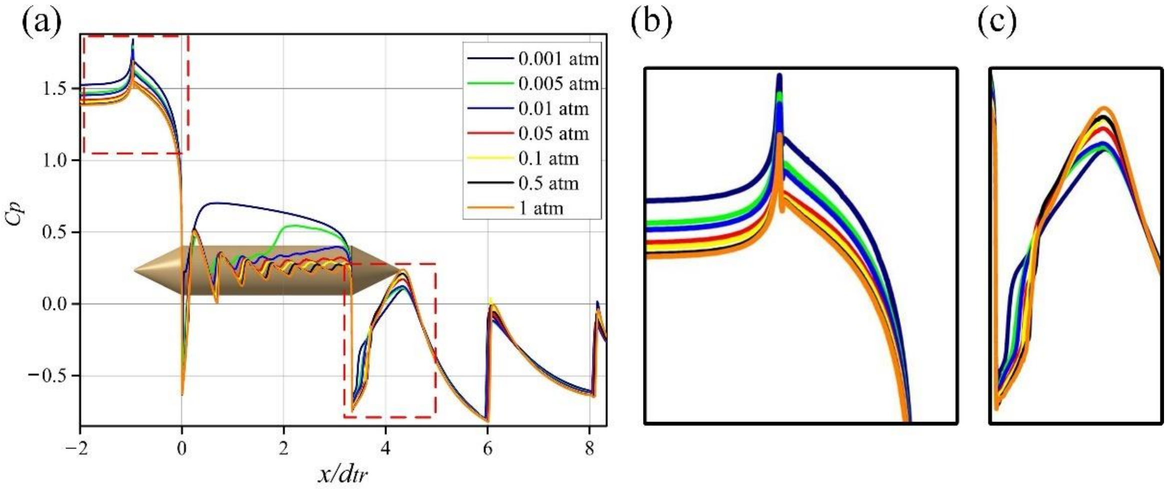

Figure 16. (**a**) The distribution of C_P along the axis of the tube and the longitudinal line on the train surface at different ambient pressures in the tube, (**b**) enlarged view of the C_P distribution in front of the train head, (**c**) enlarged view of the C_P distribution in the near weak.

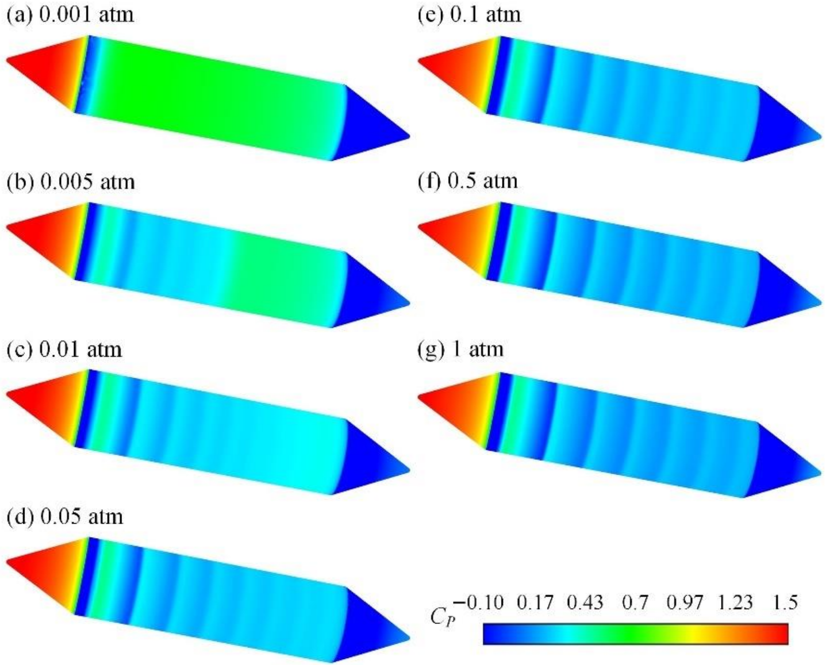

Figure 17. C_P contours on the surface of tube train.

In conclusion, the relationship between the drag and ambient pressure is approximately linear, not only at the subsonic speed but also at supersonic speed. Different ambient pressure in the tube does not change the flow structures in front of the train head and in the wake of the train tail, but some distinctions are observed around the tube train. For these reasons, the aerodynamic characteristic of ETT system can generally represent others, which are only different in ambient pressure. Meanwhile, the drag of others can be inferred roughly by the known one.

4. Conclusions

In this study, the aerodynamic characteristics of the three-dimensional ETT system were numerically investigated using RANS based on the $\kappa-\omega$ SST model. Firstly, a comparison between the ETT system and the open system was made to find out the superiority of the ETT system. Then, the effect of the travelling speed on the aerodynamic characteristics of a tube train from subsonic to supersonic was explored. Lastly, the impact of the ambient pressure in the tube of the ETT system was investigated. The main conclusions drawn in this study are as follows:

Compared with the open system, the ETT system shows a considerable drag reduction effect with suitable operating parameters in the tube, and a higher proportion of drag reduction is acquired at a higher travelling speed. Of particular interest here is that the 200 m/s case with less drag reduction shows completely different flow topology from other systems.

The relationship between the drag and travelling speed of the ETT trains demonstrates different growth tendency at different range of speed from the subsonic to supersonic speeds, which corresponds to various flow structures. In addition, the higher pressure in front of the train head due to the higher choking, and the low pressure in the wake due to the expansion waves will lead to rapid increase in the drag and the C_d. The maximum C_d appears with the strongest expansion wave occurring in the wake at Ma = 0.72.

The relationship between the drag and ambient pressure was approximately linear, not only at the subsonic speed but also at supersonic speed. Furthermore, the key flow structures were found at different ambient pressures, which verifies that this approximately linear relationship is reasonable. However, some minor distinctions were observed around the train under different ambient pressures in the tube. A low ambient pressure occurred at higher C_P in front of the train head, along with an early shock wave in the wake but without any wave reflection on the train carriage.

The above findings can lay the foundation for future studies aimed at reducing the drag of the tube train by optimizing the structure of ETT system, although a simple axisymmetric model was chosen here due to the tube train having a non-uniform shape. In addition, the track of the tube train was not taken into account. For future work, a more complex structure of the ETT system is must be investigated. Especially, the design on how to reduce the flow accumulated in front of train head and the intensity of expansion wave occurred in the wake for choking cases, is worthy of studying. Additionally, a train with a compressor may be a potential choice, as mentioned by Musk [6].

Author Contributions: Conceptualization, methodology, Z.Z., C.X., X.S., Z.Y.; validation, formal analysis, investigation, Z.Z.; resources, Z.Y., X.S.; data curation, writing—original draft preparation, Z.Z.; writing—review and editing, C.X., Z.Z.; visualization, Z.Z.; supervision, X.S.; project administration, X.S., Z.Y.; funding acquisition, Z.Y., X.S. All authors have read and agreed to the published version of the manuscript.

Funding: This research was funded by the Shanghai Key Laboratory of Aerodynamics and Thermal Environment Simulation for Ground Vehicles (18DZ2273300), the Shanghai Automotive Wind Tunnel Technical Service Platform (19DZ2290400), and National Natural Science Foundation of China (51875411).

Acknowledgments: This work was supported by the Shanghai Key Laboratory of Aerodynamics and Thermal Environment Simulation for Ground Vehicles (Grant No. 18DZ2273300), and the Shanghai Automotive Wind Tunnel Technical Service Platform (Grant No. 19DZ2290400).

Conflicts of Interest: No potential conflict of interest was reported by the authors.

References

1. Hammitt, A.G.; Systems, T.; Beach, R. Aerodynamic analysis of tube vehicle systems. *AIAA J.* **1971**, *10*, 282–290. [CrossRef]
2. Oster, D. Evacuated Tube Transport. US Patent US5950543A, 14 September 1999.
3. Zhang, Y.P. Evacuated tube transportation (ETT)—A new opportunity for vacuum industry. *Vacuum* **2006**, *43*, 56–69.
4. Van-Goeverden, K.; Milakis, D.; Janic, M.; Konings, R. Analysis and modelling of performances of the HL (hyperloop) transport system. *Eur. Transp. Res. Rev.* **2018**, *10*, 41. [CrossRef]
5. Jiang, J.; Bai, X.; Wu, L. Design consideration of a super-high speed high temperature superconductor maglev evacuated tube transport (I). *J. Mod. Transp.* **2012**, *20*, 108–114. [CrossRef]
6. Musk, E. *Hyperloop Alpha*; Space X: Hawthorne, CA, USA, 2013.
7. Wong, F.T.H. *Aerodynamic Design and Optimization of a Hyperloop Vehicle*; The Delft University of Technology: Delft, The Netherlands, 2018.
8. Shen, Z.Y. Dynamic interaction of high speed maglev train on girders and its comparison with the case in ordinary high speed railways. *J. Traffic Transp. Eng.* **2001**, *1*, 1–6.
9. Giegel, J. Making hyperloop a reality: Virgin hyperloop one. *Glob. Rail. Rev* **2018**, *24*, 28–31.
10. Abdelrahman, A.S.; Sayeed, J.; Youssef, M.Z. Hyperloop transportation system: Analysis, design, control, and implementation. *IEEE Trans. Ind. Electron.* **2018**, *65*, 7427–7436. [CrossRef]
11. Roshan, P.; Aditya, K. Vehicle dynamics of permanent-magnet levitation based hyperloop capsules. In Proceedings of the ASME 2018 Dynamic Systems and Control Conference, Atlanta, GA, USA, 30 September–3 October 2018; DSCC2018-9130.
12. Dorta, A.V.; Becker, E. The potential short-term impact of a hyperloop service between San Francisco and Los Angeles on airport competition in California. *Transp. Policy* **2018**, *71*, 45–56. [CrossRef]
13. Kang, H.; Jin, Y.; Kwon, H.; Kim, K. A study on the aerodynamic drag of transonic vehicle in evacuated tube using computational fluid dynamics. *Int. J. Aeronaut. Space Sci.* **2017**, *18*, 614–622. [CrossRef]
14. Chin, J.C. Open-source conceptual sizing models for the hyperloop passenger pod. In Proceedings of the 56th AIAA/ASCE/AHS/ASC Structures, Structural Dynamics, and Materials Conference, Kissimmee, FL, USA, 5–9 January 2015.
15. Cai, Y.G.; Chen, S.S. Dynamic characteristics of magnetically levitated vehicle systems. *Appl. Mech. Rev. ASME* **1997**, *50*, 647–670. [CrossRef]
16. Piechna, J. Low pressure tube transport—An alternative to ground road transport—Aerodynamic and other problems and possible solutions. *Energies* **2021**, *14*, 3766. [CrossRef]
17. Edwards, L.K. High-Speed Tube Transportation. *Sci. Am.* **1965**, *213*, 30–41. Available online: https://www.jstor.org/stable/24931968 (accessed on 11 April 2019). [CrossRef]
18. Axhausen, K.W. *SwissMetro*; Travel Survey Metadata Series; ETH Zürich: Zürich, Switzerland, 2013; Volume 42. [CrossRef]
19. Bierlaire, M. The acceptance of modal innovation: In Proceedings of the Case of Swissmetro. Swiss Transport Research Conference, Ascona, Switzerland, 1–3 March 2001.
20. Oster, D.; Kumada, M.; Zhang, Y.P. Evacuated tube transport technologies (ET3)tm: A maximum value global transportation network for passengers and cargo. *J. Mod. Transp.* **2011**, *19*, 42–50. [CrossRef]
21. Wang, Z.T. China is developing a 4000 km/h high speed airplane train. *Light Alloy. Fabric. Technol.* **2018**, *46*, 33.
22. Kim, T.K.; Kim, K.H.; Kwon, H.B. Aerodynamic characteristics of a tube train. *J. Wind Eng. Ind. Aerodynam.* **2011**, *99*, 1187–1196. [CrossRef]
23. Mi, B.G.; Zhan, H.; Zhu, J. Simulation of aerodynamic drag of high-speed train in evacuated tube transportation. *Chin. J. Vacuum Sci. Technol.* **2013**, *33*, 877–882.
24. Ma, J.Q.; Zhou, D.J.; Zhao, L. The approach to calculate the aerodynamic drag of maglev train in the evacuated tube. *J. Mod. Transp.* **2013**, *21*, 200–208. [CrossRef]
25. Oh, J.S.; Kang, T.; Ham, S. Numerical analysis of aerodynamic characteristics of hyperloop system. *Energies* **2019**, *12*, 518. [CrossRef]
26. Le, T.T.G.; Jang, K.S.; Lee, K.S.; Ryu, J. Numerical investigation of aerodynamic drag and pressure waves in hyperloop systems. *Mathematics* **2020**, *8*, 100–111. [CrossRef]
27. Niu, J.Q.; Sui, Y.; Yu, Q.J. Numerical study on the impact of Mach number on the coupling effect of aerodynamic heating and aerodynamic pressure caused by a tube train. *J. Wind Eng. Ind. Aerodynam.* **2019**, *190*, 100–111. [CrossRef]
28. Niu, J.Q.; Sui, Y.; Yu, Q.J. Effect of acceleration and deceleration of a capsule train running at transonic speed on the flow and heat transfer in the tube. *Aerosp. Sci. Technol.* **2020**, *105*, 105977. [CrossRef]
29. Zhou, P.; Zhang, J.Y.; Li, T. Effects of blocking ratio and Mach number on aerodynamic characteristics of the evacuated tube train. *Int. J. Rail Transp.* **2019**, *8*, 27–44. [CrossRef]
30. Chen, X.Y. Aerodynamic simulation of evacuated tube maglev trains with different streamlined designs. *J. Mod. Transp.* **2012**, *20*, 115–120. [CrossRef]
31. Zhang, Y.P. Numerical simulation and analysis of aerodynamic drag on a subsonic train in evacuated tube transportation. *J. Mod. Transp.* **2012**, *20*, 44–48. [CrossRef]
32. Wang, J.K.; Zhang, Y.; Hu, X. Aerodynamic characteristics of high-temperature superconducting maglev-evacuated tube transport. In Proceedings of the 2020th IEEE International Conference on Applied Superconductivity and Electromagnetic Devices, Tianjin, China, 16–18 October 2020.
33. Debler, W.R. *Fluid Mechanics Fundamentals*; Prentice Hall: Englewood Cliffs, NJ, USA, 1990.

34. Tong, B.G.; Kong, X.Y.; Deng, G.H. *Aerodynamics*; Higher Education Press: Beijing, China, 2012.
35. Kantrowitz, A.; Donaldson, C.D. *Preliminary Investigation of Supersonic Diffusers*; National Advisory Committee for Aeronautics: Edwards, CA, USA, 1945.
36. Kim, K.K. The Russian version of the transport system 'Hyperloop'. *Transp. Syst. Technol.* **2018**, *4*, 73–91. [CrossRef]
37. Bose, A.; Viswanathan, V. Mitigating the piston effect in high-speed hyperloop transportation: A study on the use of aerofoils. *Energies* **2021**, *14*, 464. [CrossRef]
38. Opgenoord, M.M.; Caplan, P.C. Aerodynamic design of the hyperloop concept. *AIAA J.* **2018**, *56*, 4261–4270. [CrossRef]
39. Braun, J.; Sousa, J.; Pekardan, C. Aerodynamic design and analysis of the hyperloop. *AIAA J.* **2017**, *55*, 4053–4060. [CrossRef]
40. Gillani, S.A.; Panikulam, V.P.; Sadasivan, S.; Zhang, Y.P. CFD analysis of aerodynamic drag effects on vacuum tube trains. *J. Appl. Fluid Mech.* **2019**, *12*, 303–306. [CrossRef]
41. Zhou, K.Y.; Ding, G.F.; Wang, Y.M.; Niu, J.Q. Aeroheating and aerodynamic performance of a transonic hyperloop pod with radial gap and axial channel: A contrastive study. *J. Wind Eng. Ind. Aerodynam.* **2021**, *212*, 104591. [CrossRef]
42. Hu, X.; Deng, Z.G.; Zhang, W.H. Effect of cross passage on aerodynamic characteristics of super-high-speed evacuated tube transportation. *J. Wind Eng. Ind. Aerodynam.* **2021**, *211*, 104562. [CrossRef]
43. Menter, F.R.; Kuntz, M.; Langtry, R. Ten years of industrial experience with the SST turbulence model. *Turbul. Heat Mass Transf.* **2003**, *4*, 625–632.
44. Tsien, H.S. Super-aerodynamics, mechanics of rare field gases. *J. Aerodynam. Sci.* **1964**, *13*, 653–664. [CrossRef]
45. Winter, K.G.; Rotta, J.C.; Smith, K.G. Studies of the Turbulent Boundary Layer on a Waisted Body of Revolution in Subsonic and Supersonic Flow. Aeronautical Research Council Reports & Memoranda. 1968. Available online: https://reports.aerade.cranfield.ac.uk/handle/1826.2/2902 (accessed on 22 June 2020).